

ADVANCED ENERGY MATERIALS

Supporting Information

for *Adv. Energy Mater.*, DOI 10.1002/aenm.202404151

High-Performance Quasi-Solid-State Thermogalvanic Cells with Metallized Fibril-Based Textile Electrodes and Structure-Breaking Salts

Jaejin Choi, Jeongmin Mo, Jaemin Jung, Yeongje Jeong, Jinhan Cho and Jaeyoung Jang**

Supporting Information

High-Performance Quasi-Solid-State Thermogalvanic Cells with Metallized Fibril-Based Textile Electrodes and Structure-Breaking Salts

Jaejin Choi, Jeongmin Mo, Jaemin Jung, Yeongje Jeong, Jinhan Cho, and Jaeyoung Jang**

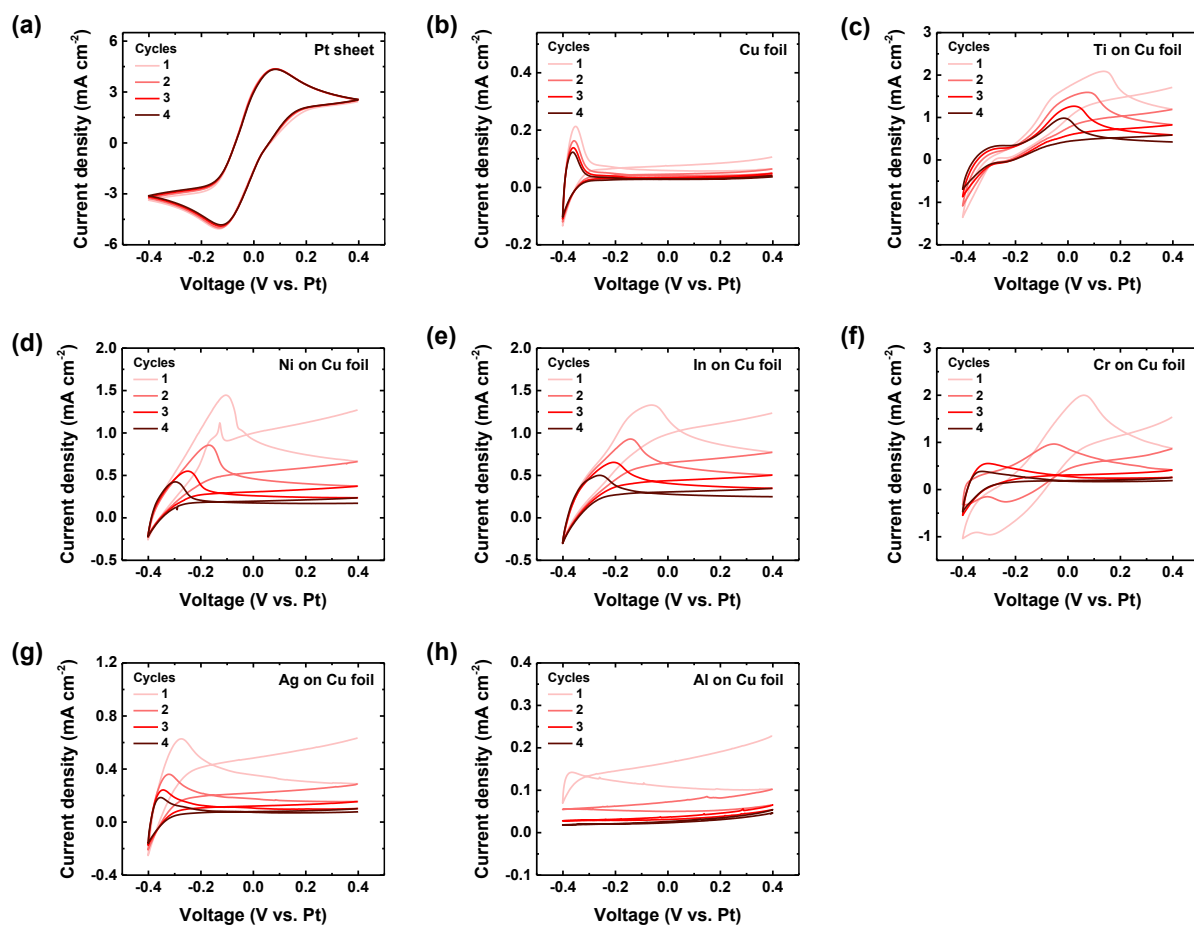


Figure S1. CV curves of different metal electrodes measured with FeCN-PAM electrolytes including 2 M guanidinium chloride: (a) Pt sheet, (b) Cu foil, and thermally deposited 50 nm-thick films of (c) Ti, (d) Ni, (e) In, (f) Cr, (g) Ag, and (h) Al on Cu foils.

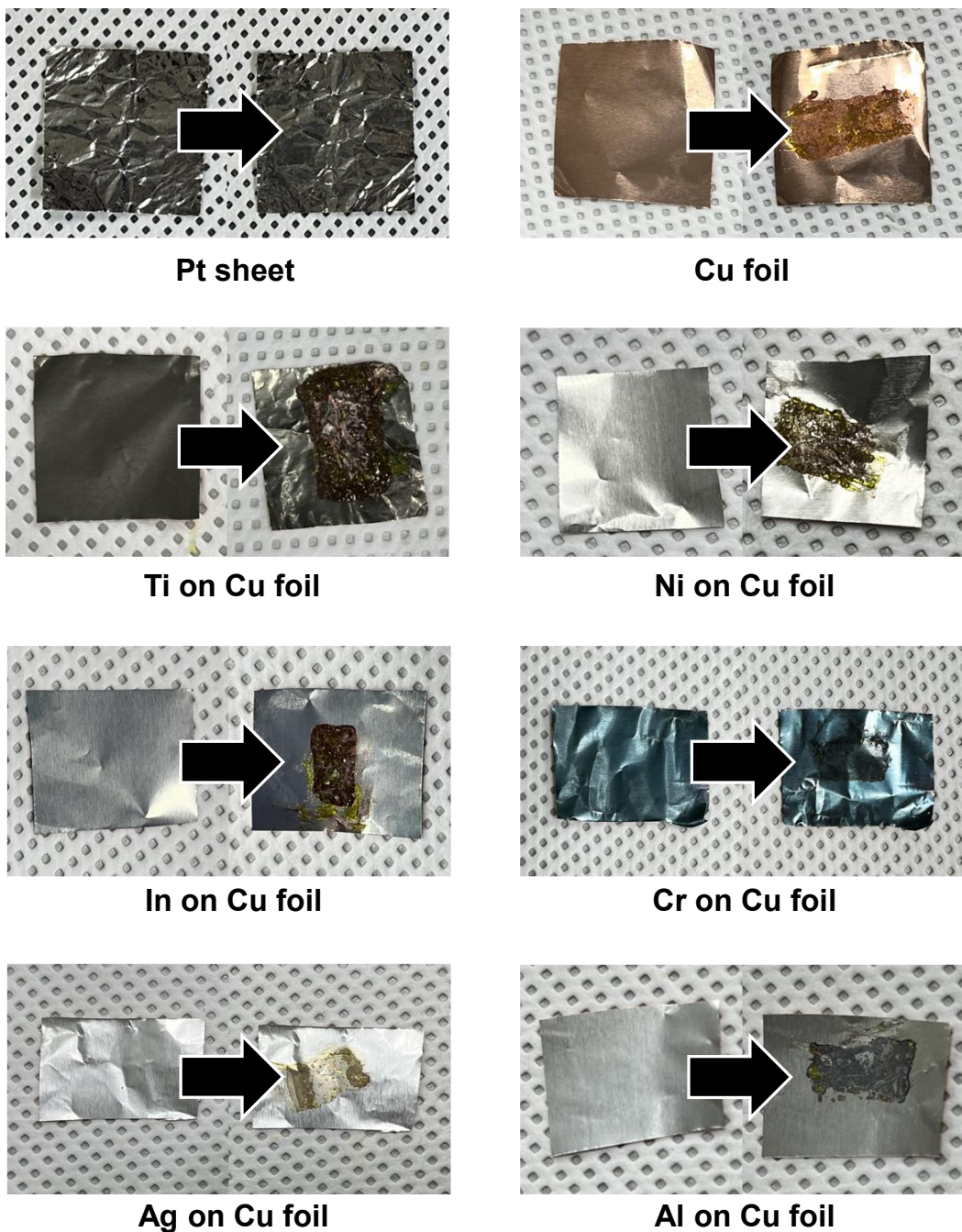


Figure S2. Photographs of the tested samples in Figure S1 before (left) and after (right) the CV measurements. The hydrogel electrolytes were detached from the electrodes after measurements, and electrolyte residues remained for the other samples except the Pt sheet sample.

Table S1. Intensity ratios of D to G bands and 2D to G bands of CCTs carbonized at different temperatures.

	550 °C	650 °C	750 °C	850 °C
I_D/I_G	0.72	0.85	0.96	1.01
I_{2D}/I_G	0.51	0.41	0.33	0.22

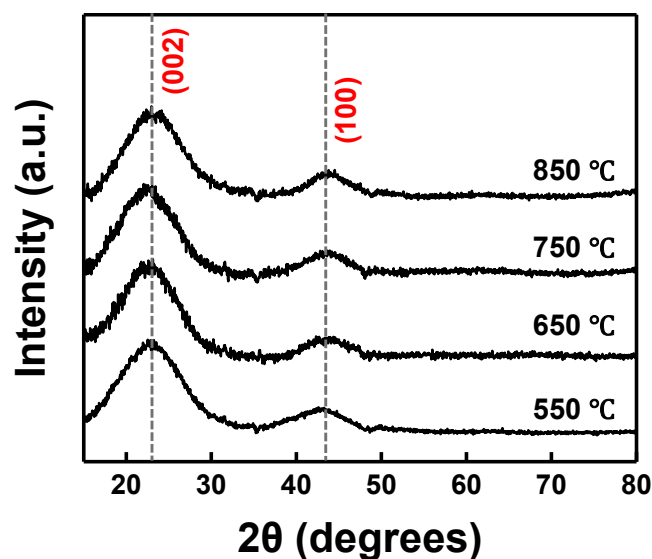


Figure S3. XRD patterns of CCTs carbonized at different temperatures.

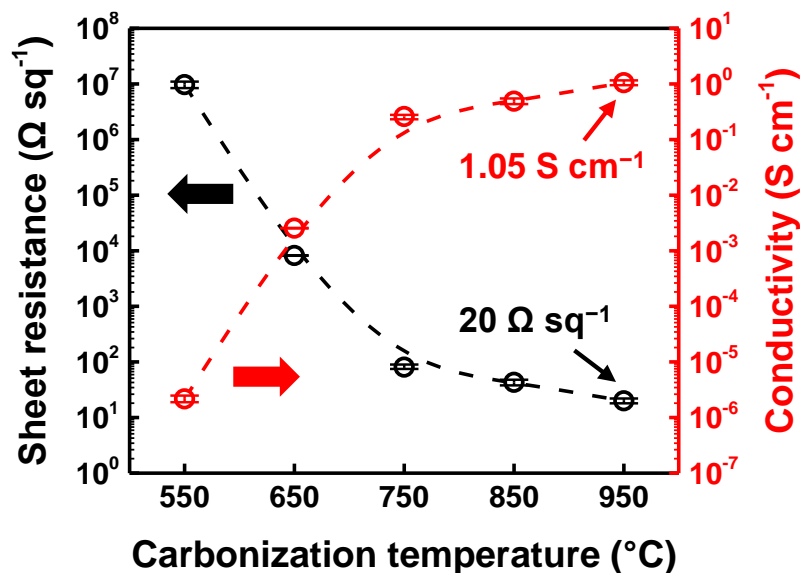


Figure S4. Sheet resistances and electrical conductivities of CCTs as functions of carbonization temperature. The CCT carbonized at 850 °C had a thickness of approximately 480 μm.

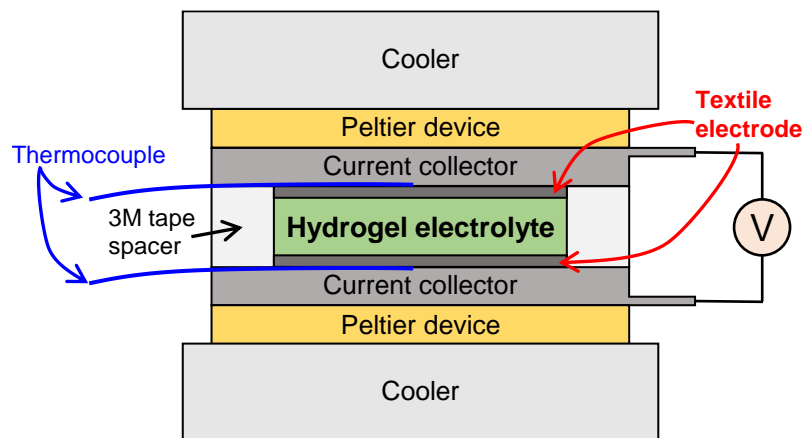


Figure S5. Schematic of a custom-built apparatus for measuring the performance of a TGC device

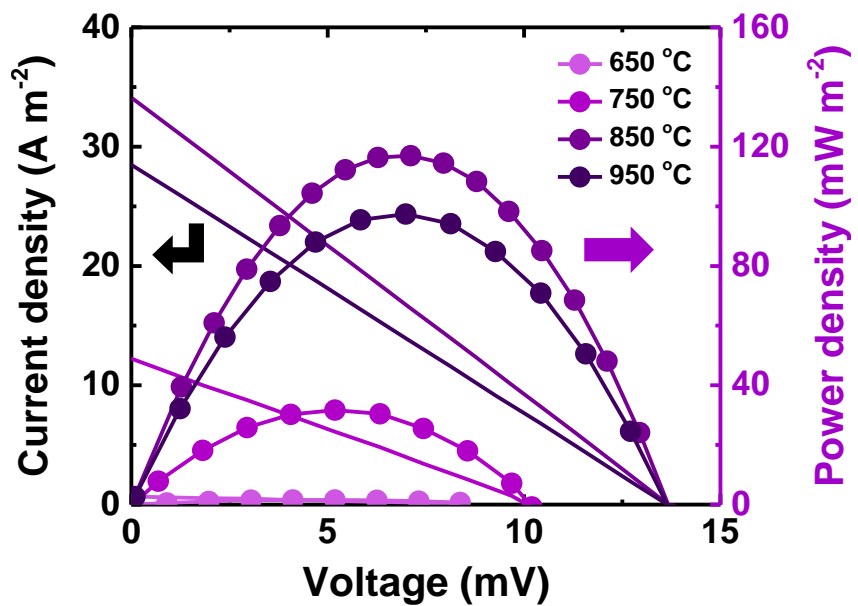


Figure S6. Output current and power densities versus input voltage of all-flexible QTCs ($\Delta T = 10 \text{ K}$) using CCT electrodes prepared with different carbonization temperatures.

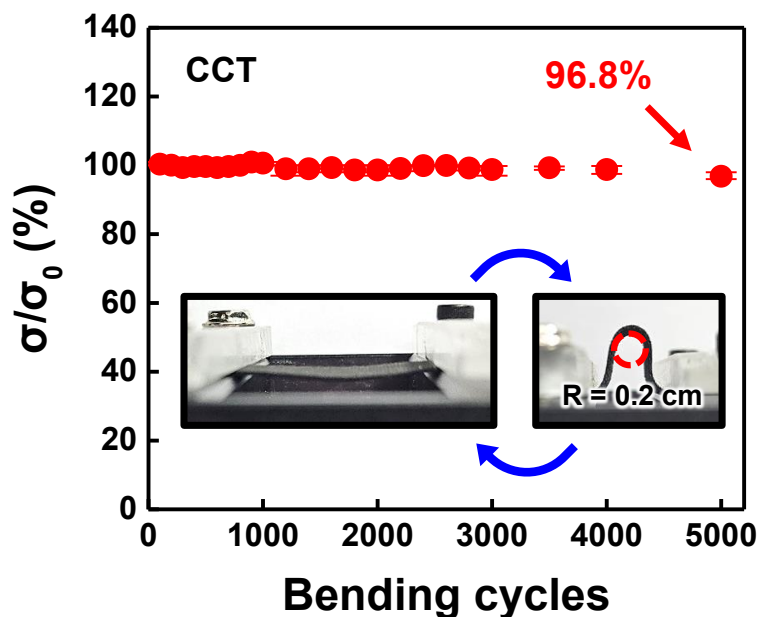


Figure S7. Plot of relative electrical conductivity (σ/σ_0) over bending cycle for CCT carbonized at 850 °C. Inset photographs show a CCT before and after bending with a bending radius (R) of 0.2 cm.

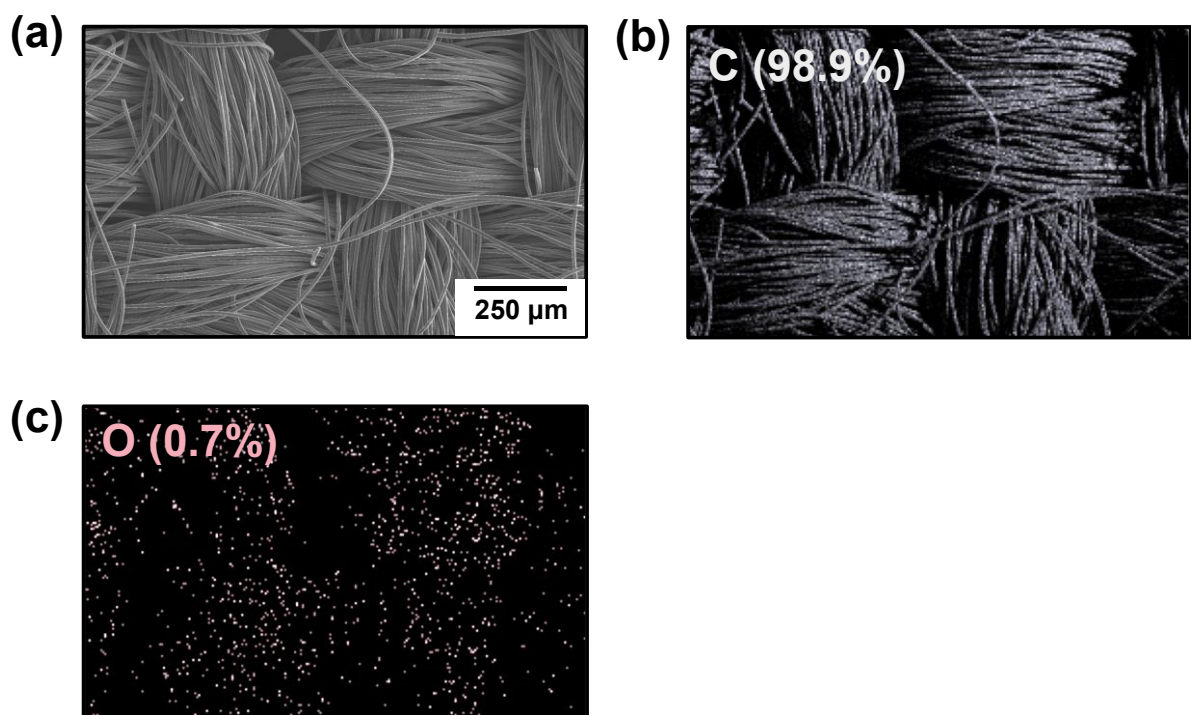


Figure S8. Images obtained from (a) FE-SEM and (b) C and (c) O EDS of commercial carbon cloth. All images share the same scale bar.

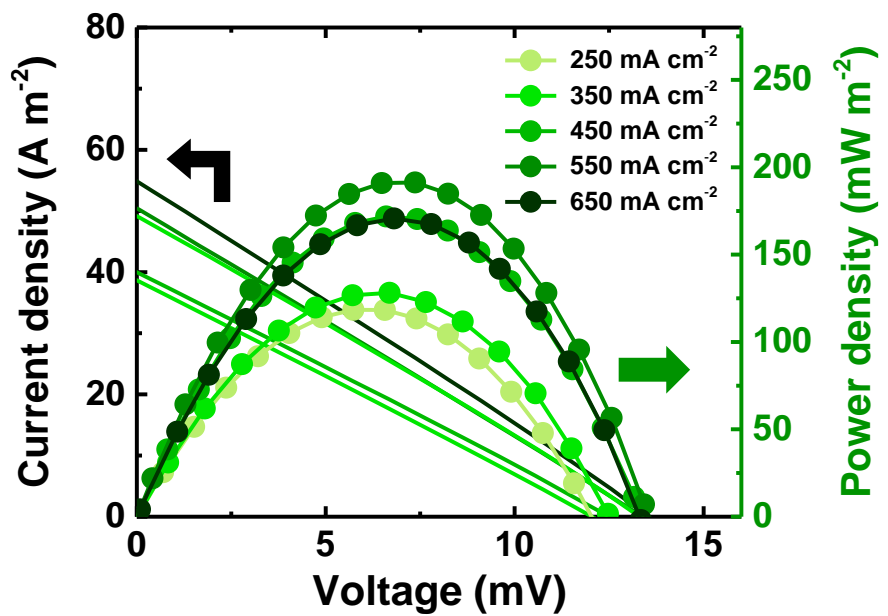


Figure S9. Output current and power densities versus input voltage of all-flexible QTCs ($\Delta T = 10 \text{ K}$) using Ni-CCT electrodes prepared with different electrodeposition current densities.

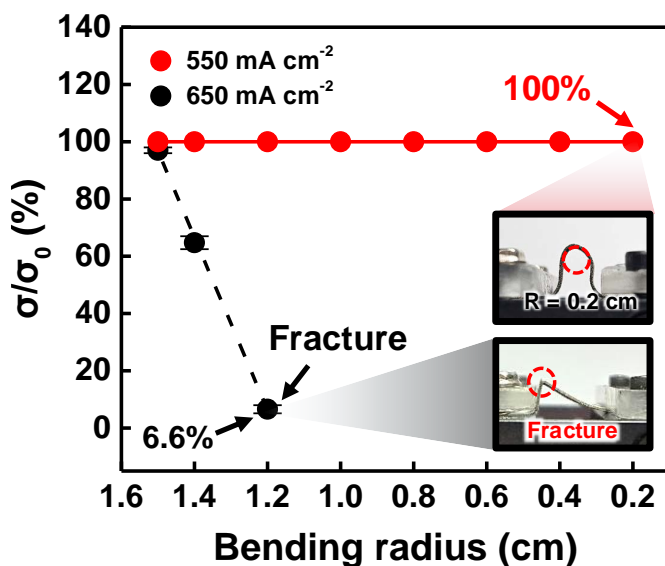


Figure S10. Plot of σ/σ_0 over bending radius for Ni-CCTs electrodeposited at 550 and 650 mA cm^{-2} . Inset photographs show two Ni-CCTs at each marked state.

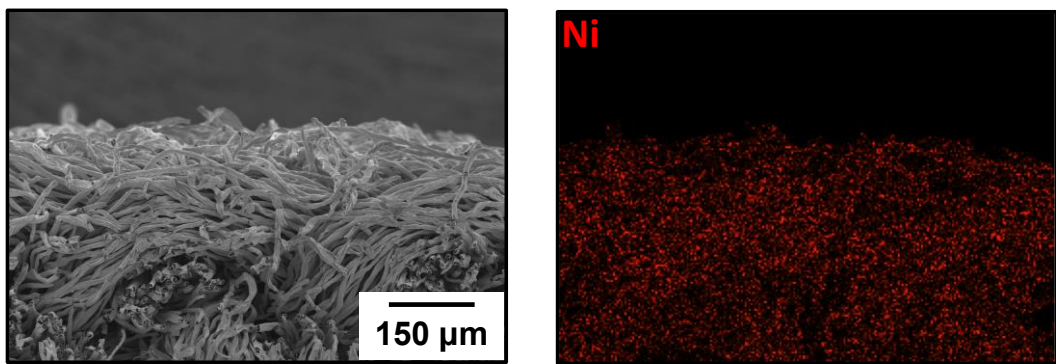


Figure S11. Cross-sectional FE-SEM (left) and EDS (Ni, right) images of Ni-CCT. Both images share the same scale bar.

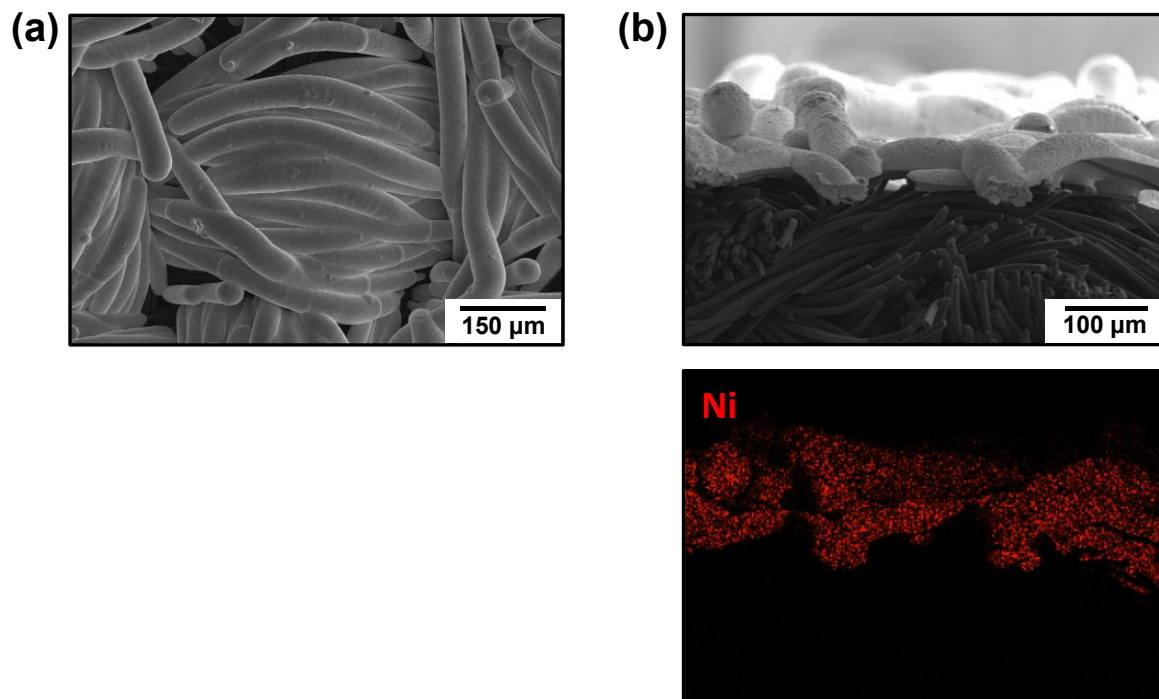


Figure S12. (a) Top-view FE-SEM image of Ni-electrodeposited carbon cloth and its (b) cross-sectional view FE-SEM (top) and EDS (Ni, bottom) images. Both images in (b) share the same scale bar.

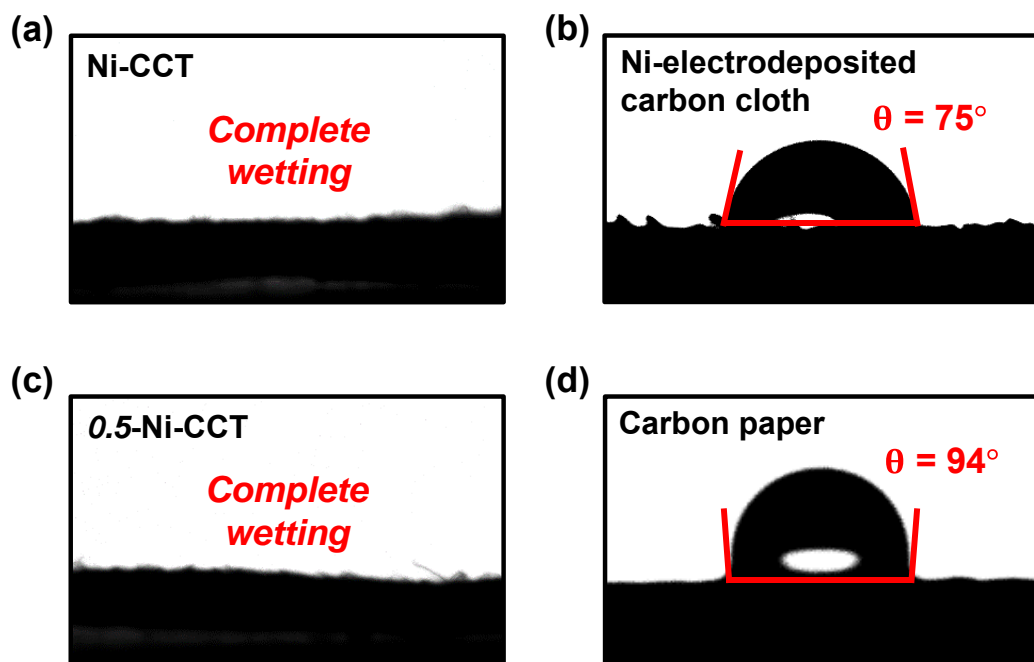


Figure S13. Water contact angle images of (a) Ni-CCT, (b) Ni-electrodeposited commercial carbon cloth, (c) 0.5-Ni-CCT, and (d) commercial carbon paper.

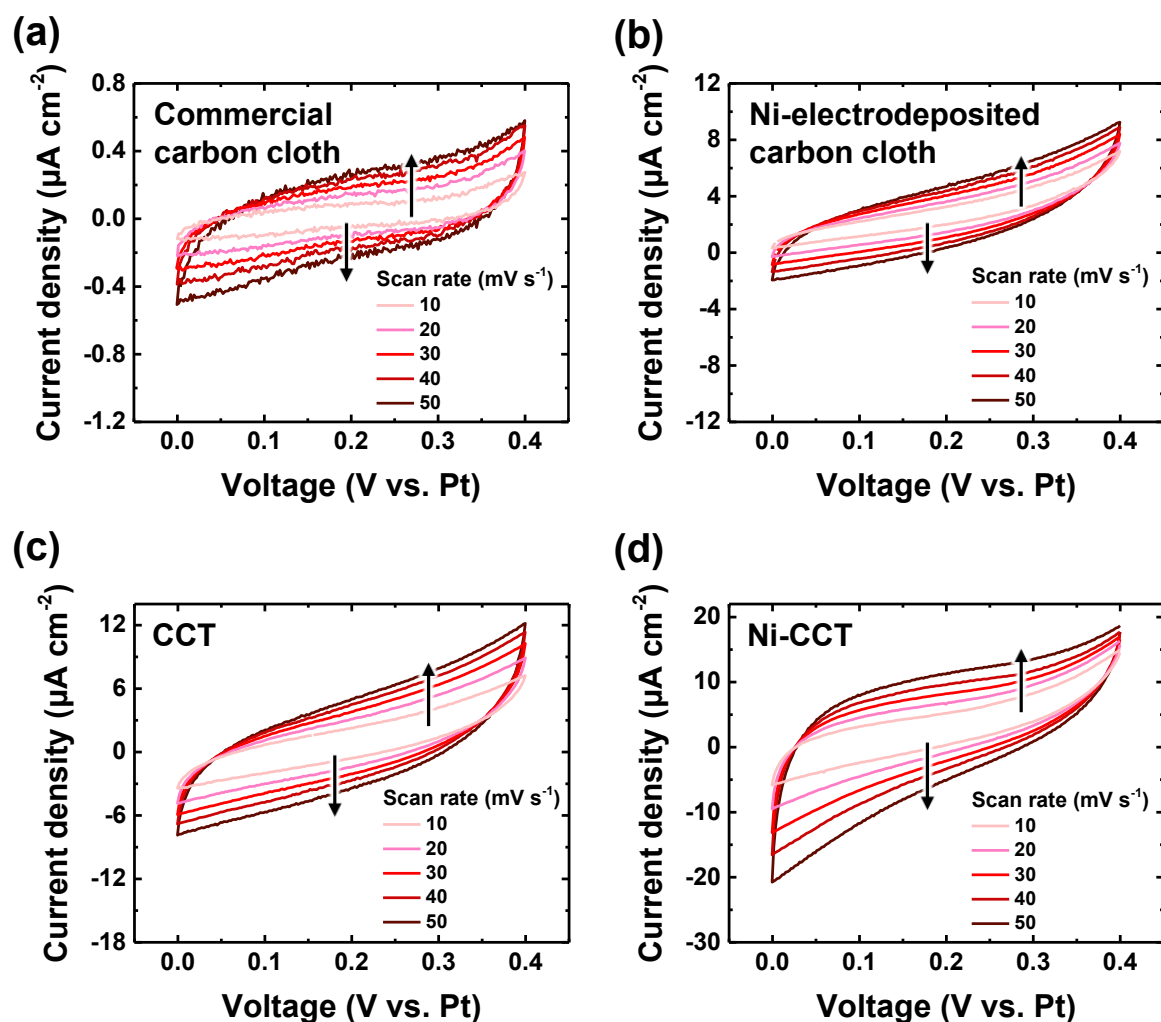


Figure S14. CV curves of (a) commercial carbon cloth, (b) Ni-electrodeposited commercial carbon cloth, (c) CCT, and (d) Ni-CCT measured at scan rates in the range of $10\text{--}50 \text{ mV s}^{-1}$.

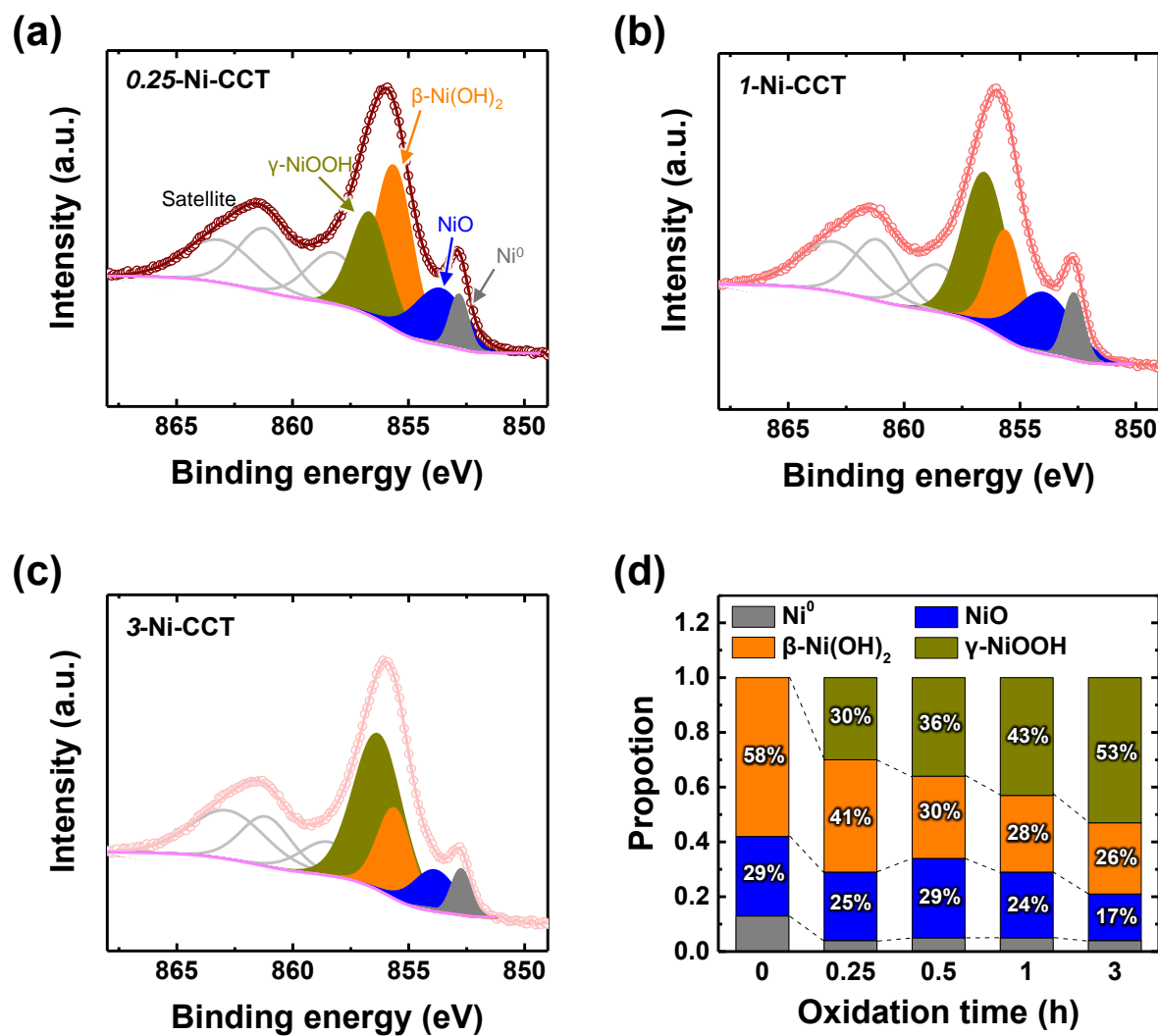


Figure S15. Ni 2p_{3/2} XPS spectra of (a) 0.25-Ni-CCT, (b) 1-Ni-CCT, and (c) 3-Ni-CCT. (d) Proportions of Ni⁰, NiO, β-Ni(OH)₂, and γ-NiOOH plotted over oxidation time.

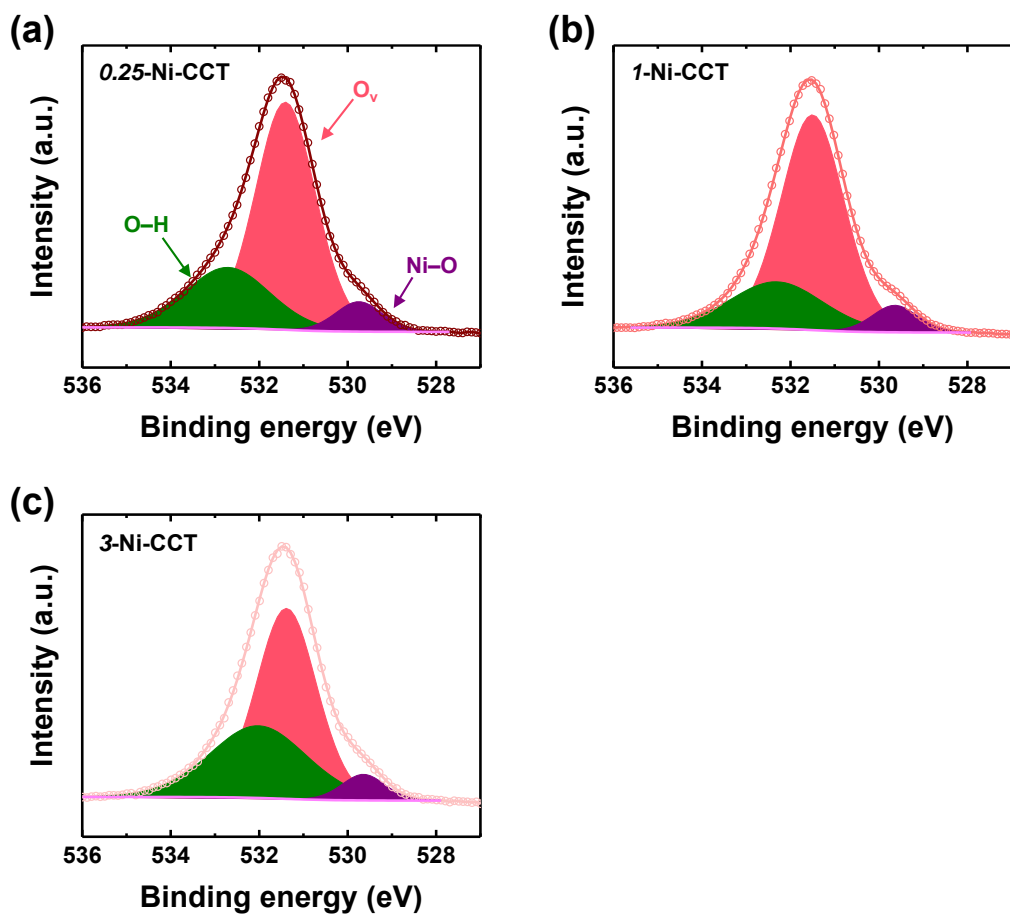


Figure S16. O 1s XPS spectra of (a) 0.25-Ni-CCT, (b) 1-Ni-CCT, and (c) 3-Ni-CCT.

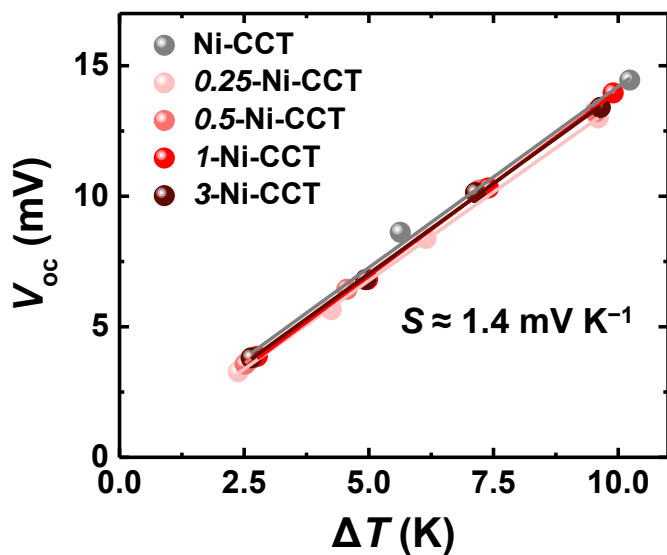


Figure S17. Plots of V_{oc} versus ΔT for all-flexible QTCs using Ni-CCT and n -Ni-CCT electrodes.

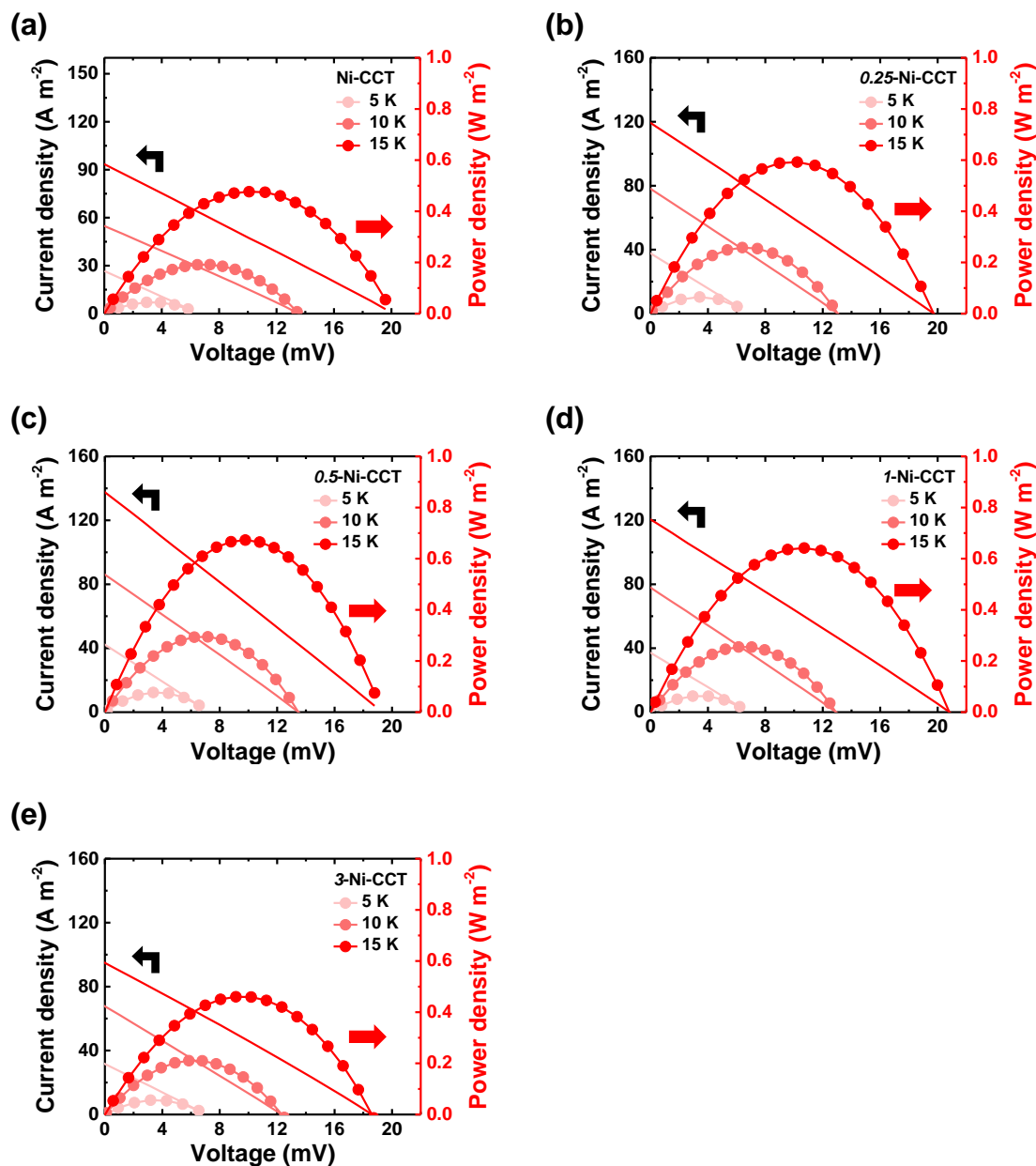


Figure S18. Output current and power densities versus input voltage of all-flexible QTCs using FeCN-PAM electrolytes and (a) Ni-CCT, (b) 0.25-Ni-CCT, (c) 0.5-Ni-CCT, (d) 1-Ni-CCT, and (e) 3-Ni-CCT electrodes measured at $\Delta T = 5, 10$, and 15 K.

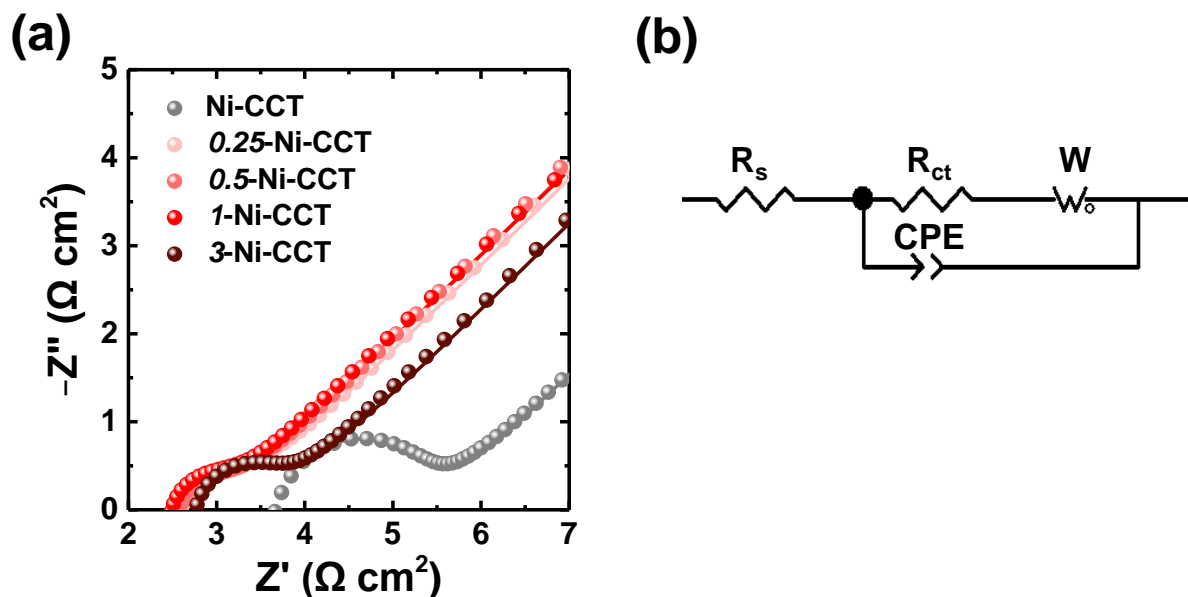


Figure S19. (a) Nyquist plots of all-flexible QTCs using Ni-CCT and n -Ni-CCT electrodes with neat FeCN-PAM electrolytes. (b) Equivalent circuit used for fitting the Nyquist plots, where R_s is solution resistance, CPE is constant phase element, and W is warburg impedance.

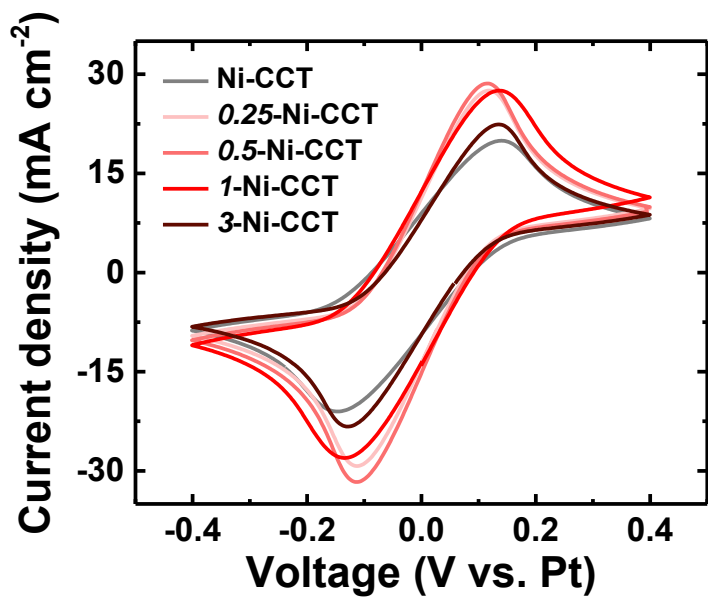


Figure S20. CV curves of all-flexible QTCs using Ni-CCT and n -Ni-CCT electrodes.

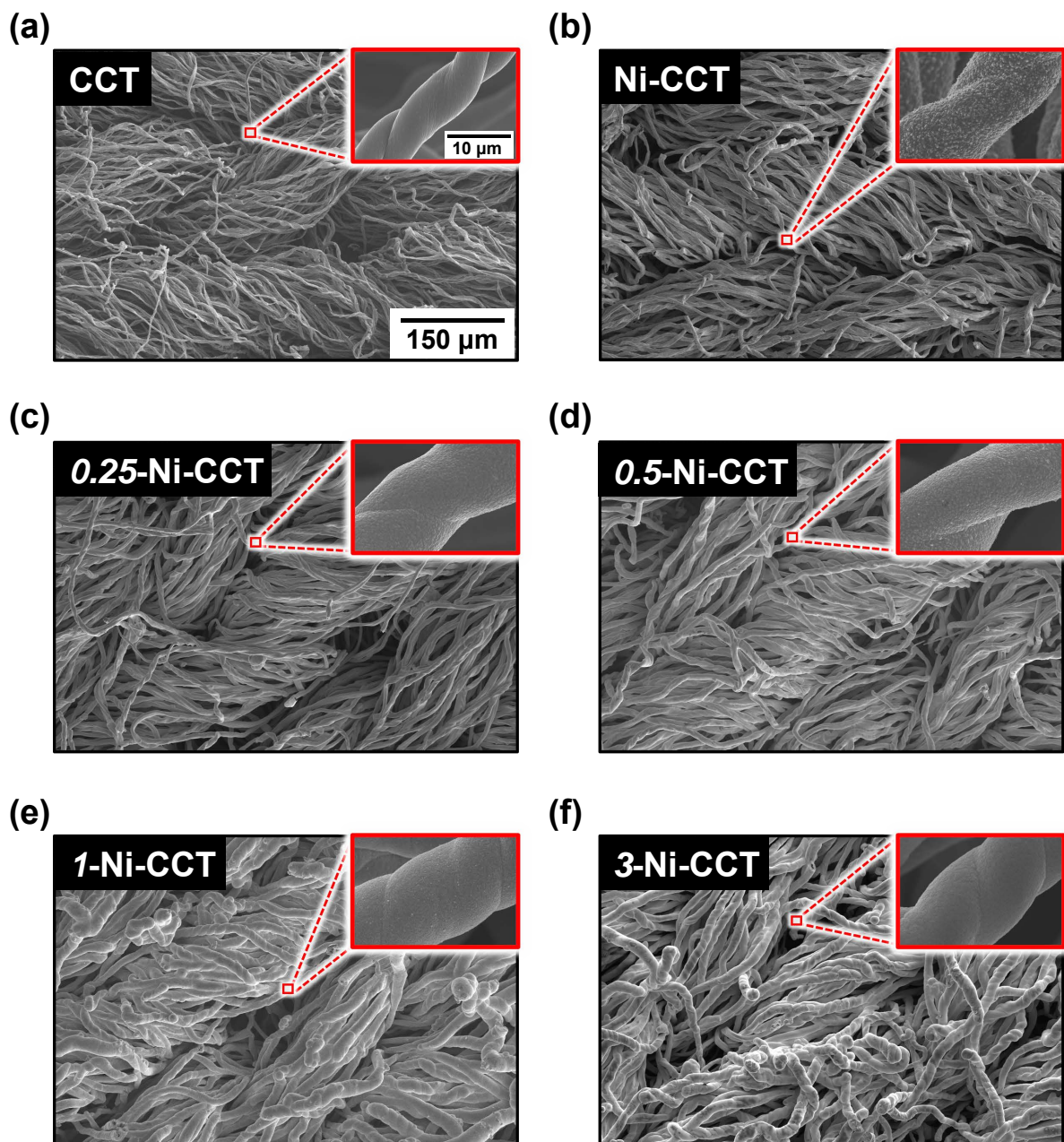


Figure S21. FE-SEM images of (a) CCT, (b) Ni-CCT, (c) 0.25-Ni-CCT, (d) 0.5-Ni-CCT, (e) 1-Ni-CCT, and (f) 3-Ni-CCT. All images share the same scale bar and insets show magnified views.

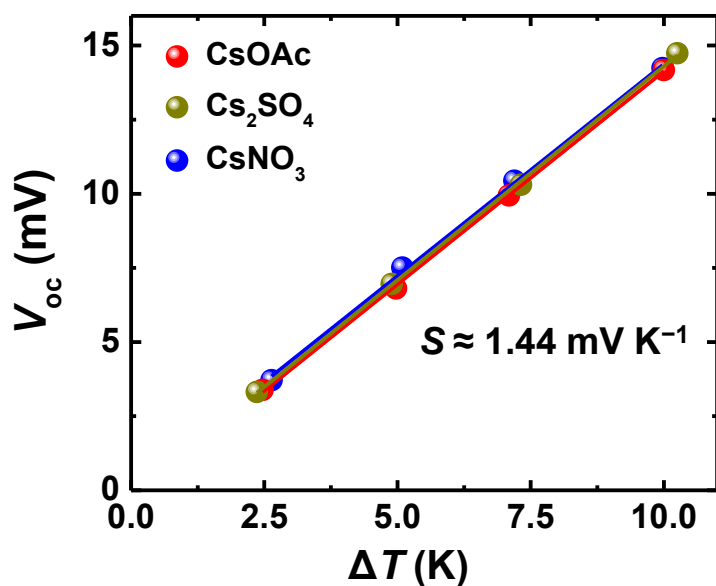


Figure S22. Plots of V_{oc} versus ΔT for all-flexible QTCs using 0.5-Ni-CCT electrodes and FeCN-PAM electrolyte with different additive salts.

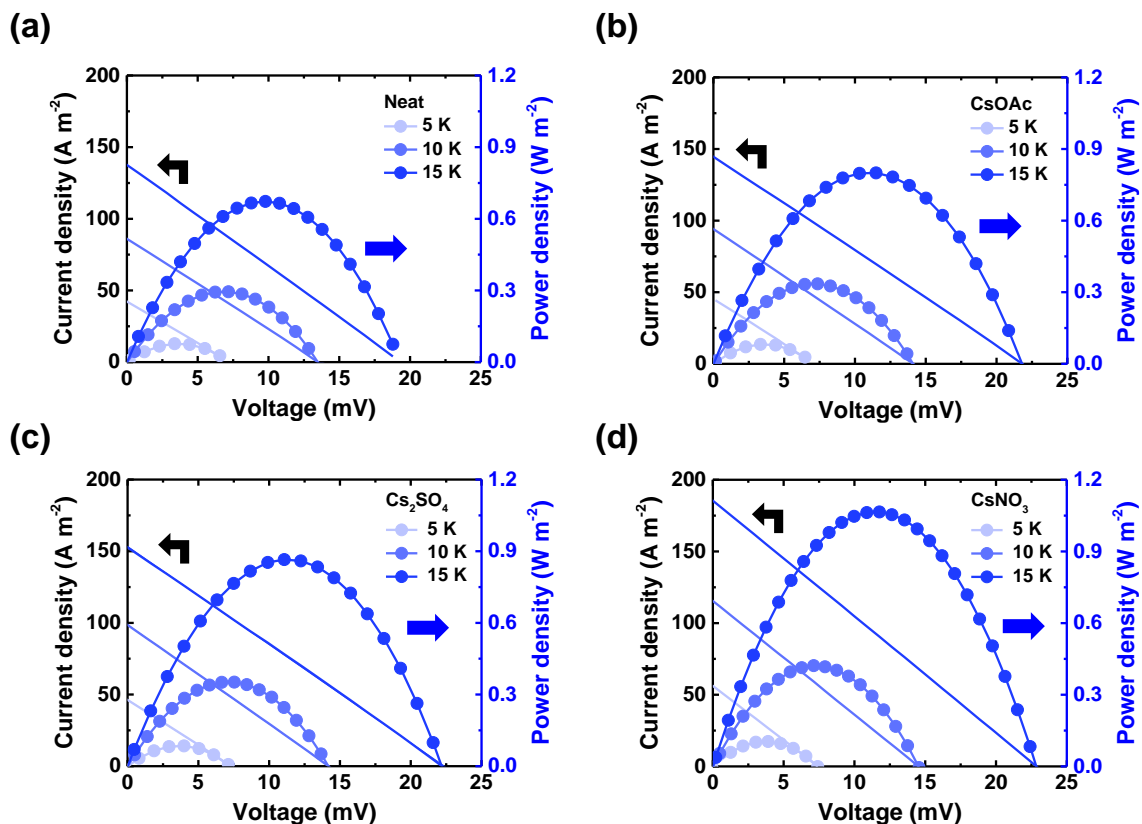


Figure S23. Output current and power densities versus input voltage of all-flexible QTCs using 0.5-Ni-CCT electrodes and FeCN-PAM electrolytes with and without additive salts measured at $\Delta T = 5, 10$, and 15 K : (a) neat, (b) CsOAc , (c) Cs_2SO_4 , and (d) CsNO_3 .

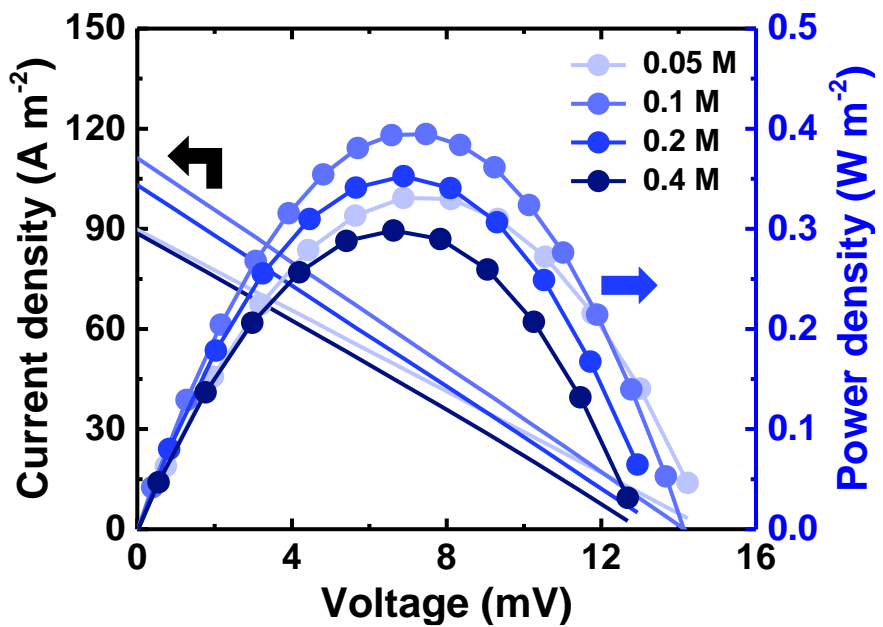


Figure S24. Output current and power densities versus input voltage of all-flexible QTCs ($\Delta T = 10 \text{ K}$) using 0.5-Ni-CCT and CsNO₃-added FeCN-PAM electrolytes with different CsNO₃ concentrations of 0.05, 0.1, 0.2, and 0.4 M.

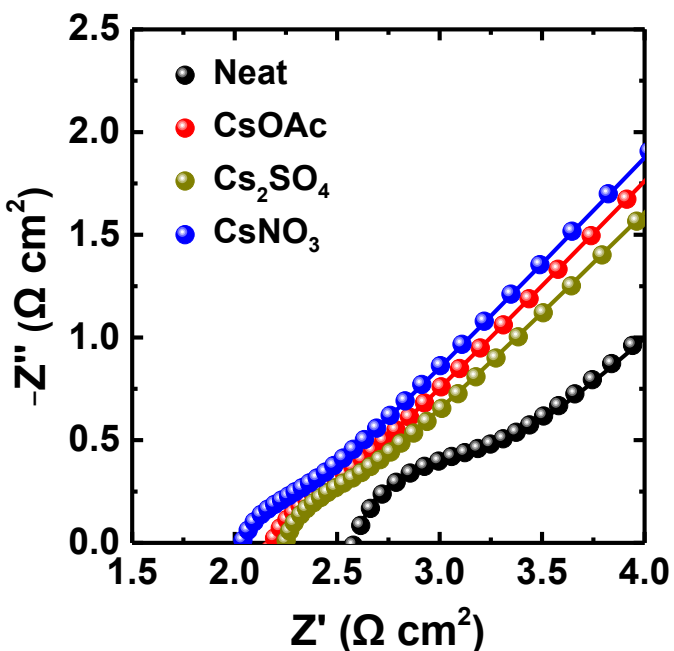


Figure S25. Nyquist plots of all-flexible QTCs using 0.5-Ni-CCT electrodes and FeCN-PAM electrolyte with and without additive salts.

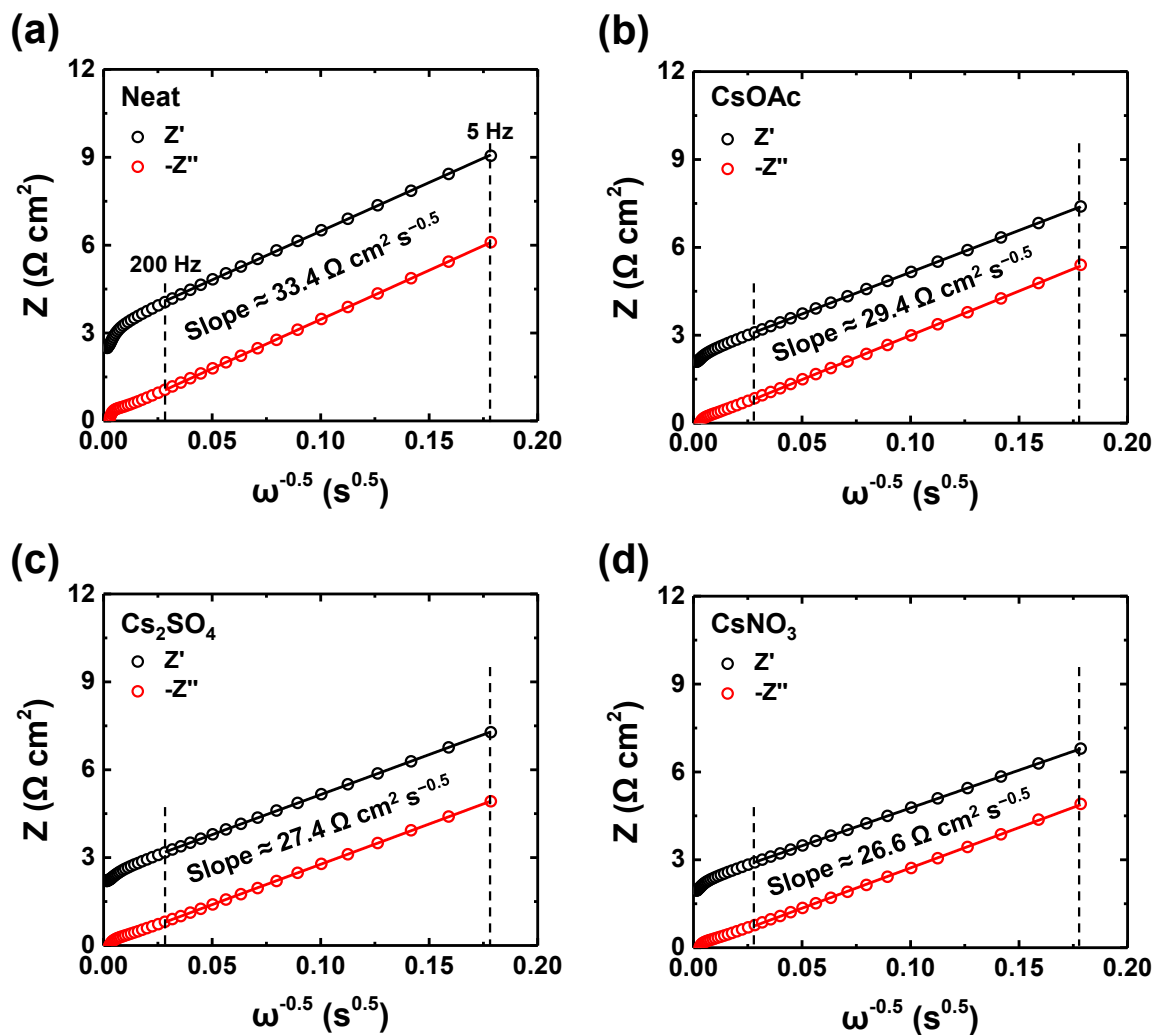


Figure S26. Warburg plots of QTCs using FeCN-PAM electrolyte (a) without any salts and with (b) CsOAc , (c) Cs_2SO_4 , and (d) CsNO_3 (ω : angular frequency).

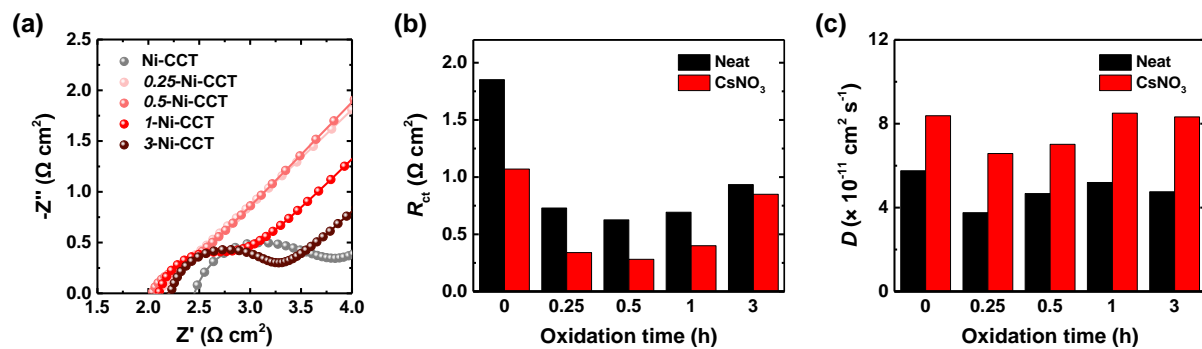


Figure S27. (a) Nyquist plots of all-flexible QTCs using CsNO_3 -added FeCN-PAM electrolytes with Ni-CCT and n -Ni-CCT ($n = 0.25, 0.5, 1$, and 3). (b) R_{ct} and (c) D of the QTCs plotted over oxidation time.

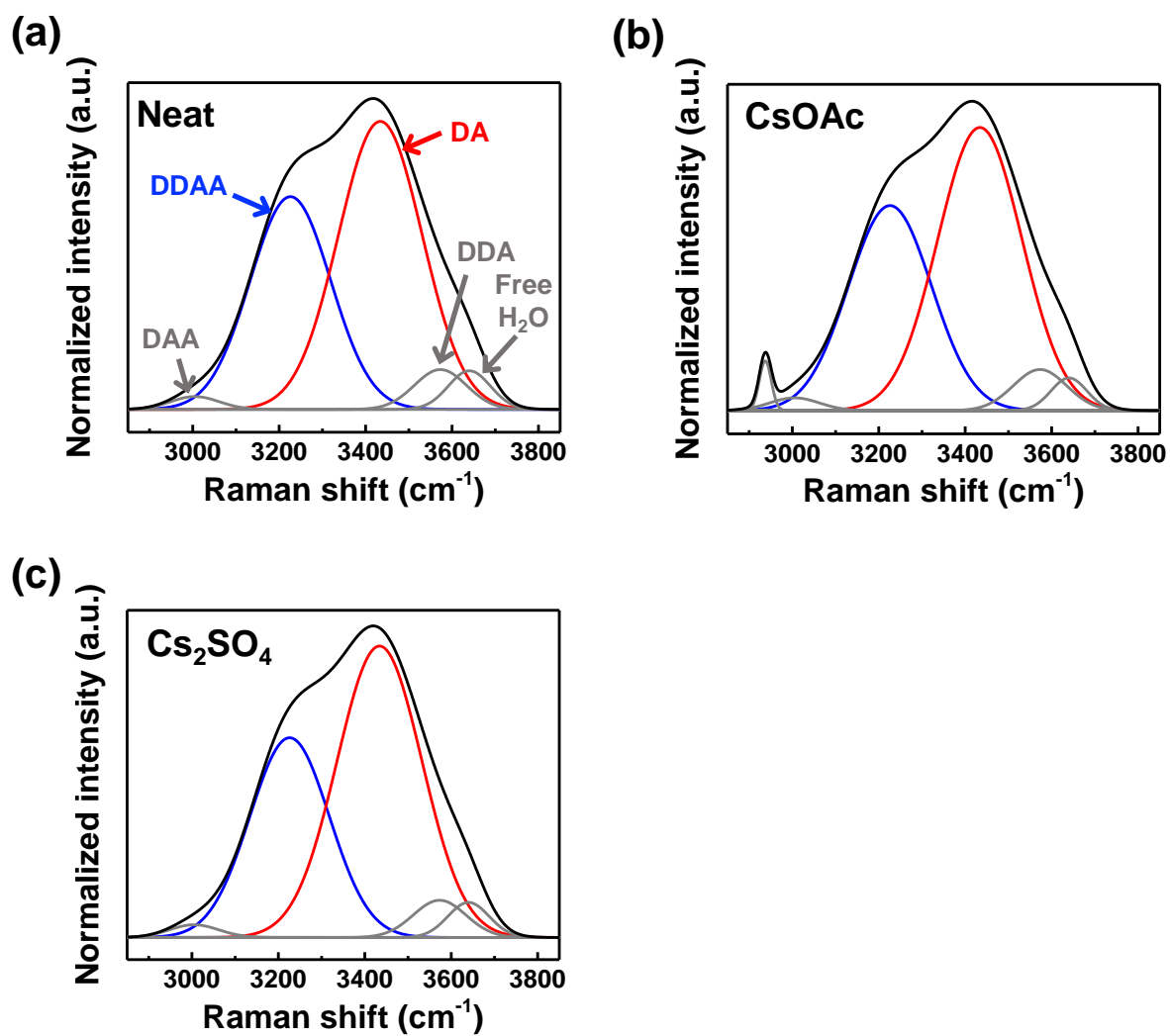


Figure S28. Raman O–H stretching spectrum and its deconvoluted spectra for aqueous potassium ferrocyanide solutions (0.01 M) (a) without any salts and with (b) CsOAc (0.8 M) and (c) Cs₂SO₄ (0.4 M).

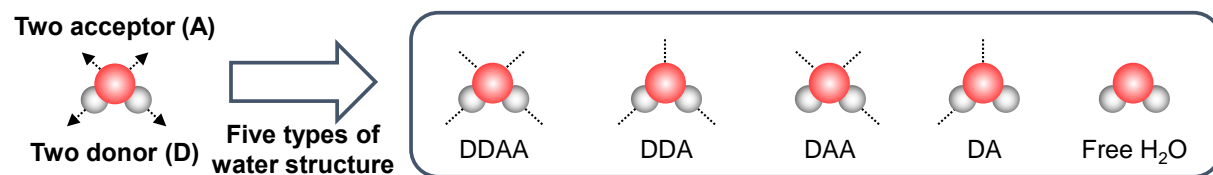


Figure S29. Schematic of five types of hydrogen-bonded water structures. Dashed lines denote hydrogen bonds.

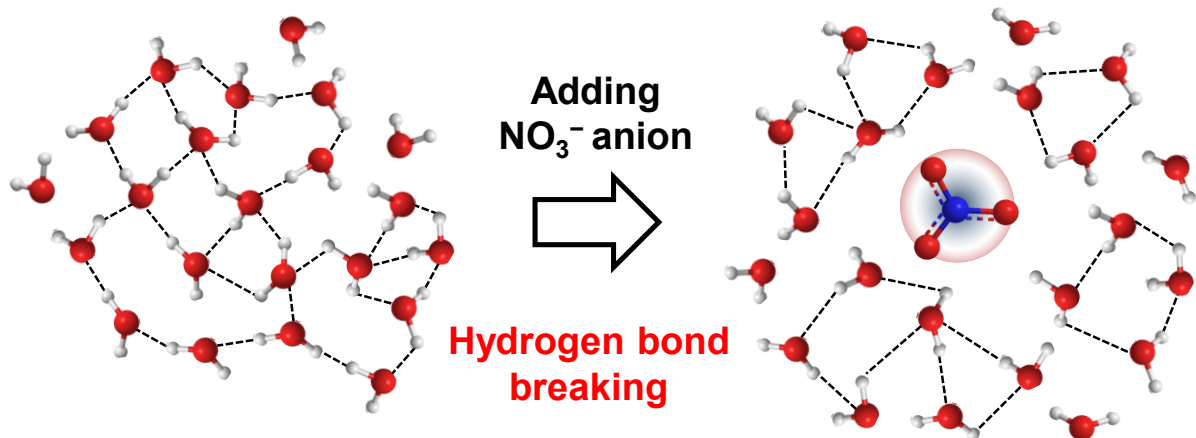


Figure S30. Schematic of breakage of hydrogen bonds of water in presence of NO_3^- anion.

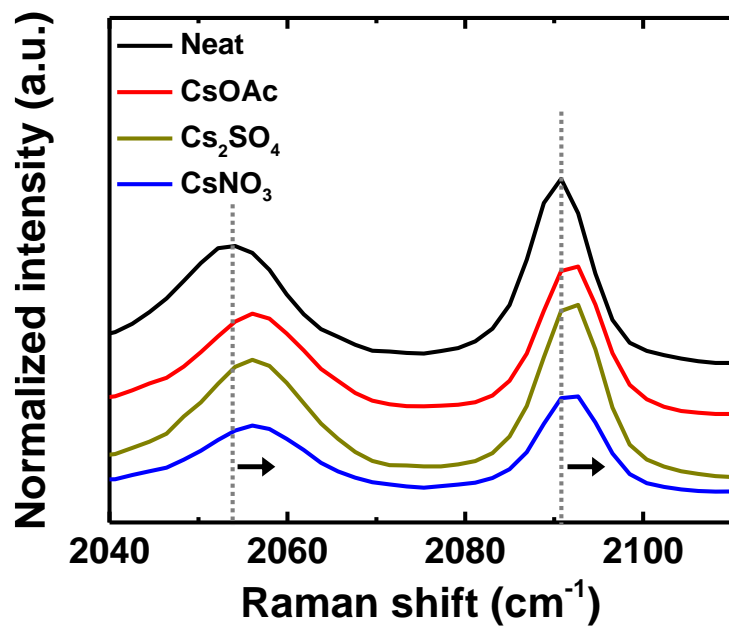


Figure S31. Raman C≡N stretching spectra of aqueous potassium ferrocyanide solution (0.01 M) without any salts (Neat) and with CsOAc (0.8 M), Cs₂SO₄ (0.8 M), and CsNO₃ (0.4 M).

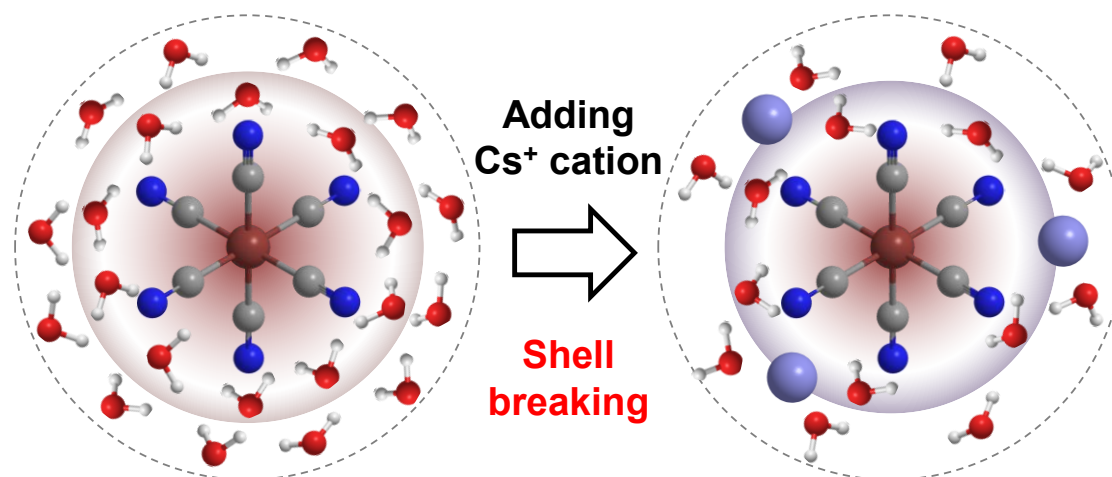


Figure S32. Schematic of breakage of FeCN hydration shell by added Cs⁺ cations.

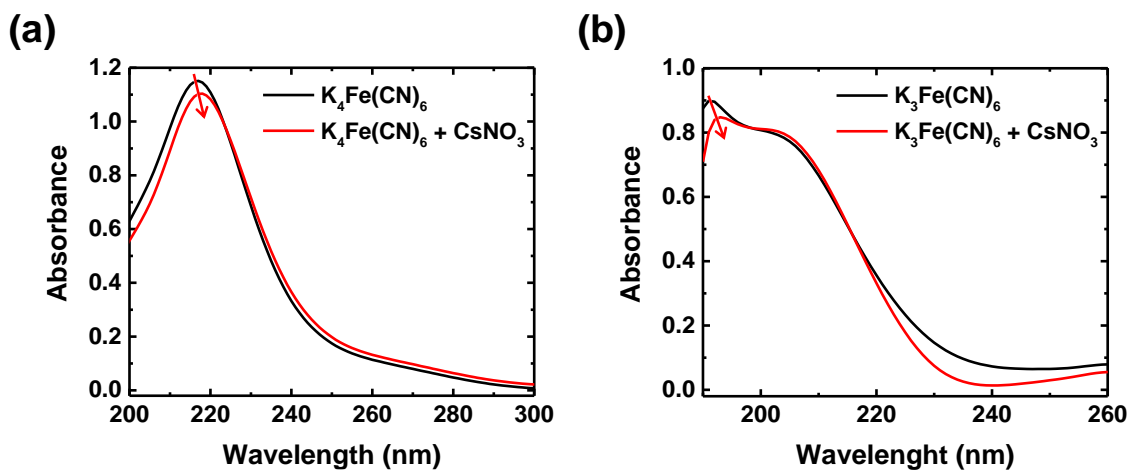


Figure S33. UV-vis spectra of (a) 0.4 M $\text{K}_4\text{Fe}(\text{CN})_6$ and 0.4 M (b) $\text{K}_3\text{Fe}(\text{CN})_6$ solutions with and without 0.1 M CsNO_3 salt.

Table S2. Performance comparison of our all-flexible QTCs with reported QTCs not using noble-metal electrodes.

Hydrogels and additives	Electrode	Redox couple	σ_{eff} (S m ⁻¹)	$P_{\text{max}}/(\Delta T)^2$ (mW m ⁻² K ⁻²)	Reference
PAM	CCT	FeCN	5.48	1.19	This work
PAM	Ni-CCT	FeCN	8.89	1.94	This work
PAM	0.5-Ni-CCT	FeCN	13.9	2.98	This work
PAM + CsNO ₃	0.5-Ni-CCT	FeCN	17.3	4.05	This work
Carboxymethyl cellulose	Laser-etched PEDOT/PSS ⁱ⁾ -EFG/CNT ⁱⁱ⁾	FeCN	3.03	0.73	[1]
PVA ⁱⁱⁱ⁾	Laser-etched PEDOT/PSS	Fe	0.4	0.38	[1]
Cellulose	Ni foil	FeCN	0.25	0.06	[2]
PAM	Graphite paper	FeCN	3.39	0.45	[3]
PAM	Graphite paper	Fe	1.02	0.3	[3]
BC ^{iv)} + Propylene glycol + Urea + LiOH	Graphene paper	FeCN	5.27	0.07	[4]
PVA/starch + PDA-HNTs ^{v)}	PEDOT/PSS-PI ^{vi)}	FeCN	4.54	0.18	[5]
BC	Carbon fiber/Cu sheet	Fe	0.22	0.156	[6]
BC/poly(acrylic acid)	Graphit paper	Fe	1.53	0.03	[7]
PVA	3D Cu foil	Cu	8	0.002	[8]
BC/PAM + GdmCl ^{vii)} + Urea	Graphene paper	FeCN	10.85	1.76	[9]

i) PEDOT/PSS: poly(3,4-ethylenedioxythiophene)/polystyrene sulfonate

ii) EFG/CNT: edge functionalized graphene/carbon nanotube

iii) PVA: polyvinyl alcohol

iv) BC: bacterial cellulose

v) PDA-HNTs: polydopamine-halloysite nanotubes

vi) PI: polyimide

vii) GdmCl: guanidinium chloride

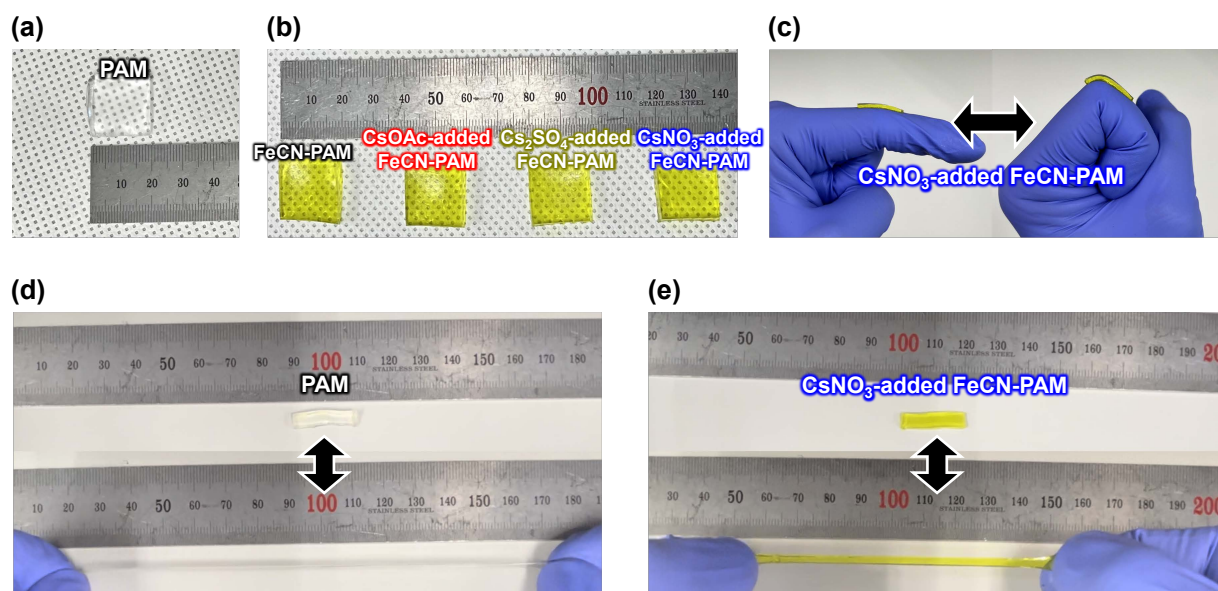


Figure S34. Photographs of (a) PAM hydrogel and (b) FeCN-PAM, CsOAc-added FeCN-PAM, Cs₂SO₄-added FeCN-PAM, and CsNO₃-added FeCN-PAM electrolytes. (c) Photograph of CsNO₃-added FeCN-PAM electrolyte attached on human finger before (left) and after (right) bending. Photographs showing stretchability of (d) PAM hydrogel and (e) CsNO₃-added FeCN-PAM electrolyte.

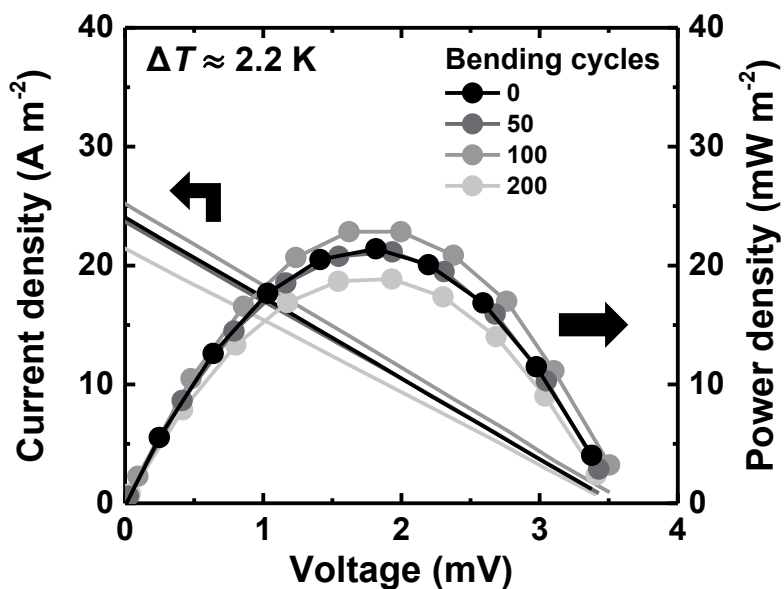


Figure S35. Output current and power densities versus input voltage of all-flexible QTC ($\Delta T \approx 2.2 \text{ K}$) using 0.5-Ni-CCT electrodes and CsNO_3 -added FeCN-PAM electrolyte before and after repeated bending (bending angle $\approx 90^\circ$).

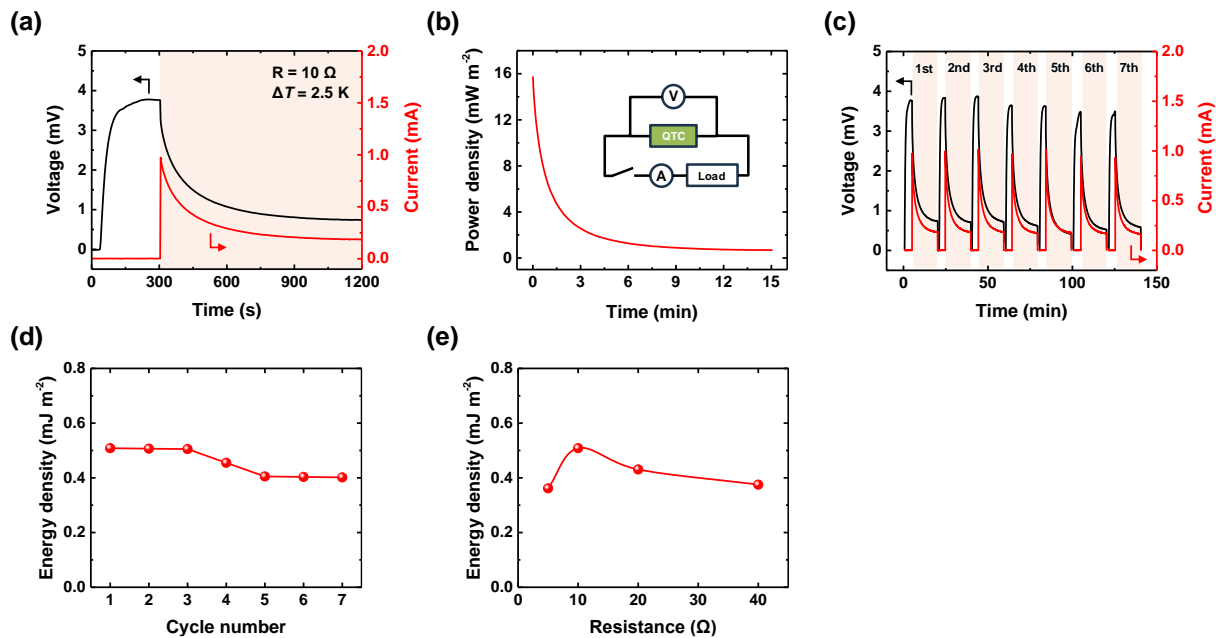


Figure S36. (a) Output voltage and current of QTC with 0.5-Ni-CCT electrodes and CsNO_3 -added FeCN-PAM electrolyte measured over time ($\Delta T = 2.5 \text{ K}$). The QTC was connected to an external resistance (10Ω) as illustrated in the circuit diagram in the inset of (b). (b) Calculated power density plotted over time. (c) Cyclic performance of output voltage and current. The measurements performed in (a) were repeated for seven cycles. (d) Output energy density harvested in 15 min plotted over cycle number. (e) Output energy density harvested in 15 min plotted over resistance value of external load.

As shown in Figure S36a, the output voltage and current of an optimized QTC was measured over time with loading an external resistance (10Ω) at $\Delta T = 2.5 \text{ K}$ until saturation (about 15 min). As a $\Delta T = 2.5 \text{ K}$ was applied, the open-circuit voltage increased to 3.65 mV in 5 min. Subsequently, the external resistance was loaded, resulting in the reduction of output voltage and the generation and decay of output current with time. Within 15 min, the output voltage and current reached a steady state. By multiplying the time-dependent output voltage and current, the output power density could be calculated and plotted over time (Figure S36b). Furthermore, we repeated the time-dependent measurements performed in Figure S36a seven times and obtained the cyclic performance of output power density and energy density, as shown in Figure S36c. The output energy density was calculated by integrating the area of

each output power density curve (Figure S36d). The external resistance value $10\ \Omega$ was determined after the energy density measurements with various resistance loads because the $10\ \Omega$ load led to the highest output energy density value (Figure S36e).

Table S3. Normalized power comparison of our all-flexible QTC with other reported QTCs and QTC modules operated using body heat or self-made platforms.

Operating ΔT (K)	Electrode	Number of units	Body heat	Normalized power ($\mu\text{W K}^{-2}$)	Reference
2	0.5-Ni-CCT	1	O	0.75	This work
4.1	Graphite paper	20	O	0.048	[3]
8.5	Pt sheet	1	O	0.028	[10]
8.5	Pt sheet	6	O	0.125	[10]
8	Graphite paper	25	O	0.05	[11]
5	3D Cu foil	4	X	0.08	[8]
5	3D Cu foil	9	X	0.16	[8]
5	3D Cu foil	18	X	0.32	[8]
2.5	Ni foam	8	X	0.218	[12]
5.1	Ni foil	3	X	0.154	[13]

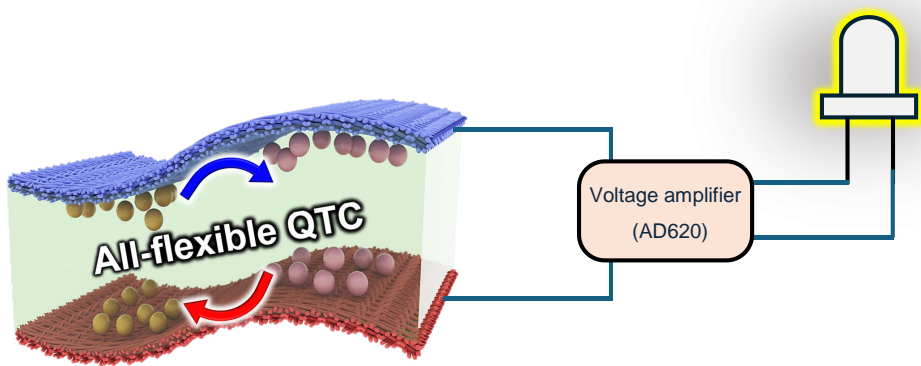


Figure S37. Schematic illustrating circuit diagram of our QTC device powering an LED *via* a voltage amplifier (AD620).

Note S1:

The *ESA* is the amount of surface area available for effective electrochemical reactions.^[14,15]

The *ESA* of each electrode (Ni-CCT and *n*-Ni-CCTs) was derived by fitting the CV data into the Randles–Sevcik equation:

$$ESA = I_p / (2.69 \times 10^5 D^{0.5} n_e^{1.5} v^{0.5} C) \quad (1)$$

where I_p is the faradaic peak current, D is the diffusion coefficient, n_e is the number of electrons transferred during the redox reaction, v is the potential scan rate, and C is the concentration of the probe molecule.

Note S2:

Generally, the low-frequency region of the Nyquist plots provide information regarding the D (diffusion coefficient) of ions in electrochemical cells.^[16,17] In this context, the D of the FeCN redox couples was evaluated by fitting the low-frequency region of the EIS data (200–5 Hz) into the following equation:

$$D = 0.5(RT)^2 / (An_e^2 F^2 CZ_w)^2 \quad (2)$$

where R is the ideal gas constant, T is the absolute temperature, A is the surface area of the interface between the electrode and the electrolyte, F is the Faraday's constant, C is the concentration of the redox couple, and Z_w is the Warburg coefficient, which is the slope of the Warburg plot in **Figure S26**.

Supplementary References

- [1] Y. Q. Liu, S. Zhang, Y. T. Zhou, M. A. Buckingham, L. Aldous, P. C. Sherrell, G. G. Wallace, G. Ryder, S. Faisal, D. L. Officer, S. Beirne and J. Chen, *Adv. Energy Mater.* **2020**, 10, 2002539.
- [2] L. Y. Jin, G. W. Greene, D. R. MacFarlane and J. M. Pringle, *ACS Energy Lett.* **2016**, 1, 654–658.
- [3] C. Xu, Y. Sun, J. J. Zhang, W. Xu and H. Tian, *Adv. Energy Mater.* **2022**, 12, 2201542.
- [4] J. Li, S. Y. Chen, Z. L. Han, X. Y. Qu, M. T. Jin, L. L. Deng, Q. Q. Liang, Y. H. Jia and H. P. Wang, *Adv. Funct. Mater.* **2023**, 33, 2306509.
- [5] N. Li, Z. Wang, X. Yang, Z. Zhang, W. Zhang, S. Sang and H. Zhang, *Adv. Funct. Mater.* **2024**, 34, 2314419.
- [6] Y. Zong, J. Lou, H. Li, X. Li, Y. Jiang, Q. Ding, Z. Liu and W. Han, *Carbohydr. Polym.* **2022**, 294, 119789.
- [7] Y. Jia, S. Zhang, J. Li, Z. Han, D. Zhang, X. Qu, S. Chen and H. Wang, *J. Power Sources* **2024**, 602, 234400.
- [8] H. Meng, W. Gao and Y. Chen, *Small* **2024**, 2310777.
- [9] Z. Wu, B. Wang, J. Li, Y. Jia, S. Chen, H. Wang, L. Chen and L. Shuai, *Nano Lett.* **2023**, 23, 10297–10304.
- [10] L. Liu, D. Zhang, P. Bai, Y. Mao, Q. Li, J. Guo, Y. Fang and R. Ma, *Adv. Mater.* **2023**, 35, e2300696.
- [11] C. Bai, Z. Wang, S. Yang, X. Cui, X. Li, Y. Yin, M. Zhang, T. Wang, S. Sang, W. Zhang and H. Zhang, *ACS Appl. Mater. Interfaces* **2021**, 13, 37316–37322.
- [12] C. C. Hsu, Y. T. Lin, S. H. Hong, U. S. Jeng, H. L. Chen, J. Yu and C. L. Liu, *Adv. Sustain. Syst.* **2024**, 2400039.
- [13] S.-H. Hong, C.-C. Hsu, T.-H. Liu, T.-C. Lee, S.-H. Tung, H.-L. Chen, J. Yu and C.-L. Liu, *Mater. Today Energy* **2024**, 42, 101546.
- [14] P. Papakonstantinou, R. Kern, L. Robinson, H. Murphy, J. Irvine, E. McAdams, J. McLaughlin and T. McNally, *Fuller. Nanotub. Carbon Nanostruct.* **2005**, 13, 91–108.
- [15] H. Im, T. Kim, H. Song, J. Choi, J. S. Park, R. Ovalle-Robles, H. D. Yang, K. D. Kihm, R. H. Baughman, H. H. Lee, T. J. Kang and Y. H. Kim, *Nat. Commun.* **2016**, 7, 10600.
- [16] S. Xu, L. Lu, Q. Zhang, H. Zheng, L. Liu, S. Yin, S. Wang, G. Li and C. Feng, *J. Nanopart. Res.* **2015**, 17, 1–11.
- [17] Y. Sun, J. Tang, K. Zhang, X. Yu, J. Yuan, D.-M. Zhu, K. Ozawa and L.-C. Qin, *RSC Adv.* **2021**, 11, 34152–34159.